Advances in Geo-Energy Research

Vol. 17, No. 1, p. 17-29, 2025

Original article

Molecular insights into two-phase flow in clay nanopores during gas hydrate recovery: Wettability-induced multiple pathways of water lock formation

Bin Fang[1,2], Zhun Zhang[3], Qian Zhang[1], Guangjun Guo[4]*, Jianwen Jiang[5], Fulong Ning[3]*

[1]*School of Marine Science and Engineering, Hainan University, Haikou 570228, P. R. China*

[2]*Engineering Research Center of Rock-Soil Drilling & Excavation and Protection, Ministry of Education, Wuhan 430074, P. R. China*

[3]*Faculty of Engineering, China University of Geosciences, Wuhan 430074, P. R. China*

[4]*Key Laboratory of Deep Petroleum Intelligent Exploration and Development, Institute of Geology and Geophysics, Chinese Academy of Sciences, Beijing 100029, P. R. China*

[5]*Department of Chemical and Biomolecular Engineering, National University of Singapore, Singapore 117576, Singapore*

Keywords:
Natural gas hydrate
molecular dynamics simulation
two-phase flow
surface wettability
water bridge

Cited as:
Fang, B., Zhang, Z., Zhang, Q., Guo, G., Jiang, J., Ning, F. Molecular insights into two-phase flow in clay nanopores during gas hydrate recovery: Wettability-induced multiple pathways of water lock formation. Advances in Geo-Energy Research, 2025, 17(1): 17-29.
https://doi.org/10.46690/ager.2025.07.02

Abstract:
A comprehensive understanding of the intricate water/gas two-phase flow in sedimentary pores is essential for accurately predicting gas production following the *in-situ* dissociation of natural gas hydrates, as it is crucial for optimizing resource extraction strategies. This study constructed three typical clay slit nanopore models with distinct wettability characteristics – hydrophilic, relatively hydrophobic, and Janus hybrid-wettability – and used molecular dynamics simulations to investigate the spatial distribution and transport dynamics of two-phase fluids under varying water saturation conditions. The results revealed a significant negative correlation between water saturation and gas relative permeability. When water saturation reaches a critical threshold, the water lock effect occurs, blocking gas flow. Pore wettability plays a key regulatory role in water/gas phase dynamics via influencing the formation pathways of water locks. In relatively hydrophobic pores, weaker solid-water interactions promote the rapid clustering of water molecules, forming water locks, while hydrophilic surfaces enable water lock formation through gradual thickening of the liquid film. In Janus pores with low water saturation, strong electrostatic interactions between oppositely charged pore walls facilitate the formation of discrete water bridge networks, maintaining "gas windows" that allow gas flow, although these windows eventually close as saturation increases. The lower the water saturation, the more favorable it is for gas transport; in contrast, hydrophilic pores exhibit higher gas transport efficiency. Our findings provide valuable molecular-scale insights into how wettability governs multiphase flow transport, offering a theoretical foundation for reservoir modification and seepage control in natural gas hydrate recovery.

1. Introduction

Natural Gas Hydrates (NGHs) are non-stoichiometric crystalline compounds, consisting of hydrocarbon (primarily methane) guest molecules encapsulated by water molecules in polyhedral cages (Dendy and Koh, 2007). Due to their immense energy potential, NGHs are acknowledged as a prospective alternative clean energy resource (Collett et al., 2015). Various methods have been derived for exploiting NGHs,

Yandy Scientific Press

*Corresponding author.
E-mail address: fangbin126@cug.edu.cn (B. Fang); 20121003712@cug.edu.cn (Z. Zhang); qian.zhang@hainanu.edu.cn (Q. Zhang); guogj@mail.igcas.ac.cn (G. Guo); chejj@nus.edu.sg (J. Jiang); nflzx@cug.edu.cn (F. Ning).

Received May 11, 2025; revised June 8, 2025; accepted June 30, 2025; available online July 2, 2025.

including thermal stimulation, depressurization, CO_2 gas replacement, chemical additive injection, solid-state fluidized mining, etc., with depressurization being the most prevalent technique applied (Li et al., 2016; Ye et al., 2020). Most extraction techniques, except for solid-state fluidized mining, involve *in-situ* phase changes-in line with the formation and dissociation of hydrates-along with the seepage of water and gas released from dissociated hydrates. Despite substantial advancements in hydrate exploitation, significant challenges persist, including sand production (Uchida et al., 2016; Fang et al., 2023; Li et al., 2024a), secondary hydrate formation (Yang et al., 2019), clay mineral swelling due to water absorption (Low, 1980; Madsen and Müller-Vonmoos, 1989), and the deformation behavior of methane hydrate-bearing sediments by hydrate dissociation (Hyodo et al., 2013, 2014), all of which can compromise reservoir permeability, and the resultant permeability reduction may precipitate a rapid decline in gas production rates.

Relative permeability, a key factor influencing extraction efficiency, describes the flow ability of a fluid in a multiphase system. Several studies have aimed to determine the relative permeability of water/gas multiphase flow in hydrate reservoirs (Li et al., 2024b). Permeability in hydrate-bearing sediments was found to be primarily influenced by factors such as grain size, porosity, pore connectivity, water saturation, hydrate saturation, and hydrate occurrence modes (Kleinberg and Griffin, 2005; Daigle et al., 2015; Cai et al., 2020). Naturally, hydrate resources are primarily found in the pores of fine-grained marine sediments, whose sizes typically range from hundreds of nanometers to micrometers; pore throats can also be as small as a few nanometers (Boswell, 2009; Huang et al., 2023). One of the typical characteristics of natural gas hydrate reservoirs is their low porosity and permeability. Due to nanoscale effects-such as slip boundary conditions, non-continuum behavior, high specific surface area, and strong fluid-solid interactions-fluid flow in nanoscale pores deviates significantly from macroscopic flow. This deviation is governed by complex mechanisms involving the combined effects of slip flow, surface diffusion, adsorption-desorption dynamics, and possible phase transitions near pore walls, all of which are strongly influenced by the physicochemical properties of fluid and the pore surface composition (Karniadakis et al., 2005; Falk et al., 2010). Due to the coexistence and interplay of these factors, coupled with the experimental and modeling limitations, the governing mechanisms of nanofluid flow remain poorly understood, constraining our knowledge of seepage processes in sediments after hydrate dissociation.

To elucidate the relative permeability of water/gas and underlying mechanisms, it is imperative to investigate the two-phase water/gas flow dynamics within nanopores at the molecular level while taking into account the prevalence of nanopores alongside micropores in hydrate-bearing sediments. The initial distribution of hydrates and the subsequent dissociated water and gas in the reservoir cause variations in pore water saturation, leading to the formation of water bridges, particularly at narrow pore throats, thereby rapidly reducing pore connectivity and flow permeability (Holditch, 1979; Zheng et al., 2023, 2025). The formation of water bridges has become one of the decisive factors controlling gas relative permeability. However, the spatial resolution of conventional macroscopic experiments precludes the direct observation of these microscopic processes (at the nanometer scale), rendering the formation mechanisms of water bridges within pore throats obscure.

Molecular Dynamics (MD) simulations allow observing the static distribution and dynamic flow processes of water/gas two-phase systems at the molecular level within pores, providing key insights into the microscopic mechanisms of seepage. Researchers have constructed multiphase molecular configurations within pores and used MD simulations to demonstrate that in hydrophilic silica pores, water molecules preferentially adsorb onto the solid surface. As water saturation increases, water molecules aggregate to form water bridges connecting the pores. Although the migration of methane gas within pores is influenced by these water bridges, it still adheres to Darcy's law (Ho and Striolo, 2015; Liu et al., 2018). Furthermore, with increasing flow rates, these water bridges can rupture (Liu et al., 2018). Zheng et al. (2023) observed the formation of liquid "water lock" (i.e., when a water bridge completely blocks the water/gas flow in a pore), which can stop gas flow, and further analyzed the relationship between water saturation and permeability within the pores. Two-phase water/gas flow within pores is closely related to the wettability and shape of pores, and this correlation corresponds to the "pump method" developed by Guo's group (Zhang et al., 2020; Zheng et al., 2025). Xu et al. (2020) designed carbon nano-slits with adjustable surface wettability and simulated the water/gas two-phase flow within pores. The results indicated that in super hydrophilic pores, as water saturation increases, water bridges form within pores. Conversely, in super hydrophobic nanopores, water molecules aggregate to form droplets that do not contact the solid pore surface. Li et al. (2020) studied the water/gas two-phase flow in pores with different shapes and found that in square-shaped nanopores, water molecules preferentially accumulate at the corners with smaller curvature radii. Subsequently, a nearly cylindrical water interface forms on the adsorbed water layer on the pore walls to accommodate gas flow. The formation and shape of the water bridges are controlled by the electric field present between the pores (Hao et al., 2019; Xiong et al., 2020a). In water-oil systems, the formation and evolution of water bridges within nanopores are influenced by various factors such as pore surface properties, water saturation and salinity (Xiong et al., 2020b; Liu et al., 2022; Xiong and Devegowda, 2022).

Despite research advances in water/gas two-phase flow in nanopores (pore throats), several challenges remain in studying these phenomena after hydrate dissociation. Hydrate reservoirs exhibit typical heterogeneous characteristics, with skeletal surfaces displaying varying degrees of wettability that is predominantly hydrophilic (Li et al., 2021). The current molecular-scale research on the effect of surface wettability on water/gas flow is limited, often relying on modified Lennard-Jones potentials to simulate extreme hydrophilic and hydrophobic conditions (Xu et al., 2020). However, this approach deviates from the actual reservoir properties and often neglects the role of surface functional (such as hydroxyl) groups, resulting in

an incomplete understanding of the behavior of water and gas molecules, thereby restricting our comprehension of two-phase flow mechanisms within real reservoirs. Furthermore, while existing studies indicate that the varying wettability of surfaces influences the distribution of water molecules, the specific distribution states of water and gas under different saturation conditions remain insufficiently characterized. This gap in understanding limits our ability to optimize water/gas two-phase flow and continues to pose significant challenges for accurately predicting gas production rates from hydrate-bearing sediments, ultimately impacting the efficient extraction of NGH and the sustainable utilization of hydrate resources.

In addressing the above gaps, kaolinite clay minerals with varying hydrophilicity and relatively hydrophobicity (Zhang et al., 2016) are used in this study to construct three types of pore molecular configurations: hydrophilic, relatively hydrophobic, and Janus (mixed wettability). Under different water saturation conditions, the distribution characteristics of water and gas within these pores are investigated and their impact on the characteristics of two-phase water/gas flow are further analyzed. The results show that permeability is strongly correlated with pore surface wettability and water saturation, and that the mechanisms of water lock formation differ significantly among pores with different wettability. Notably, in Janus-type pores, the presence of gas windows under low water saturation conditions helps sustain gas flow. This work provides valuable theoretical insights for improving the accuracy of gas production predictions and designing reservoir modification strategies for hydrate exploitation.

2. Method

2.1 System configuration

In this work, kaolinite was selected as the nanopore wall. The unit cell of kaolinite with a chemical formula of $Al_4[Si_4O_{10}](OH)_8$ was derived from the American Mineralogist Crystal Structure Database (Downs and Hall-Wallace, 2003). Kaolinite is a 1 : 1 structured clay mineral with a hydrophilic octahedral aluminum-oxygen (gibbsite) layer (0 0 1) and a relatively hydrophobic tetrahedral silicon-oxygen (siloxane) layer (0 0 -1) linked by oxygen atoms. Its atomic composition varies across different surfaces, resulting in differences in the hydrophilicity and relatively hydrophobicity of the kaolinite surface (Zhang et al., 2016). On this basis, three different types of slit-shaped kaolinite nanopore initial MD models with different basal surface contacts were constructed: Nanopore with Siloxane-Siloxane Surface (NPss), Nanopore with Gibbsite-Gibbsite Surface (NPgg), and Nanopore with Siloxane-Gibbsite Surface (NPsg). These nanopore configurations were formed by two kaolinite sheets with 4 nm distance (pore size) and each pore sheet was built from $6 \times 9 \times 2$ kaolinite unit cells. The initial simulation box dimensions were $30.9 \times 80.0 \times 70.0$ Å^3.

For each pore type and under varying water saturation conditions, the initial quantities of water and methane molecules were determined using a hybrid MD and Grand Canonical Monte Carlo (GCMC) simulation. Initially, a certain number of water molecules were inserted randomly, a short anneal simulation was performed to make the water-containing nanopore system quickly reach equilibrium, and then the system equilibrated using a 5 ns NVT MD simulation. Next, the number of water molecules was adjusted to achieve the specific water saturation (the volume fraction of gas and water in the nanopore was calculated by the differential element method (Zheng et al., 2023)). Subsequently, methane molecules were added to the pores under specified temperature and pressure conditions via GCMC simulation, with the corresponding methane fugacity coefficients obtained from REFPROP (Eric et al., 2013). The GCMC simulations were run for 1 ns, with 100 GCMC exchanges (insertions or deletions) attempted every 100 timesteps, and the results were summarized in the Supplementary file (Table S1). This study also discusses the occurrence and flow characteristics of single-phase water and gas within the nanopores. For cases where the pore space is fully occupied by gas molecules ($S_w = 0$), the number of gas molecules was directly determined using GCMC simulations without the addition of water molecules. For cases where the pore space is fully occupied by water molecules ($S_w = 1.0$), the number of water molecules was calculated on the basis of water density. Finally, an NVT simulation of the two-phase pore systems with different water saturations was performed for 10 ns, and the last 5 ns of the trajectory was used for analysis (the simulation systems reached good equilibrium within the first 5 ns, as evidenced by the system energy profiles shown in Fig. S1 of the Supplementary file). After generating the exact number of CH_4 molecules under specified formation conditions (with the temperature and pressure set to the average values of the South China Sea hydrate reservoir, 287 K and 14 MPa) (Qin et al., 2020), the equilibrium configurations of the binary mixture inside kaolinite nanopores were obtained by Equilibrium Molecular Dynamics (EMD) simulation (shown in Fig. 1).

2.2 External field nonequilibrium MD simulations

For the directional flow of water/gas molecules in the pores, external field non-equilibrium molecular dynamics (EF-NEMD) simulations were conducted by loading a driving force in water and methane molecules along the pore direction (y), where the driving force is determined by pressure difference and can be calculated by the following equation (Zhang et al., 2021a; Lyu et al., 2023):

$$f_w = S_w \frac{\nabla p_y A_{xz}}{N_w} \times 1.4386 \times 10^{-4} \quad (1)$$

$$f_m = (1 - S_w) \frac{\nabla p_y A_{xz}}{N_m} \times 1.4386 \times 10^{-4} \quad (2)$$

where f_w and f_m represent the driving force added in water and methane molecules, respectively, kcal/(mol Å); S_w denotes the water saturation; A_{xz} denotes the cross area of the kaolinite nanopore, Å^2; N_w and N_m respectively represent the number of water and methane molecules in nanopores. In EF-NEMD simulations, an additional force f is added in water/gas molecules in the y direction (along the flow direction), thus, the calculation of temperature of water and

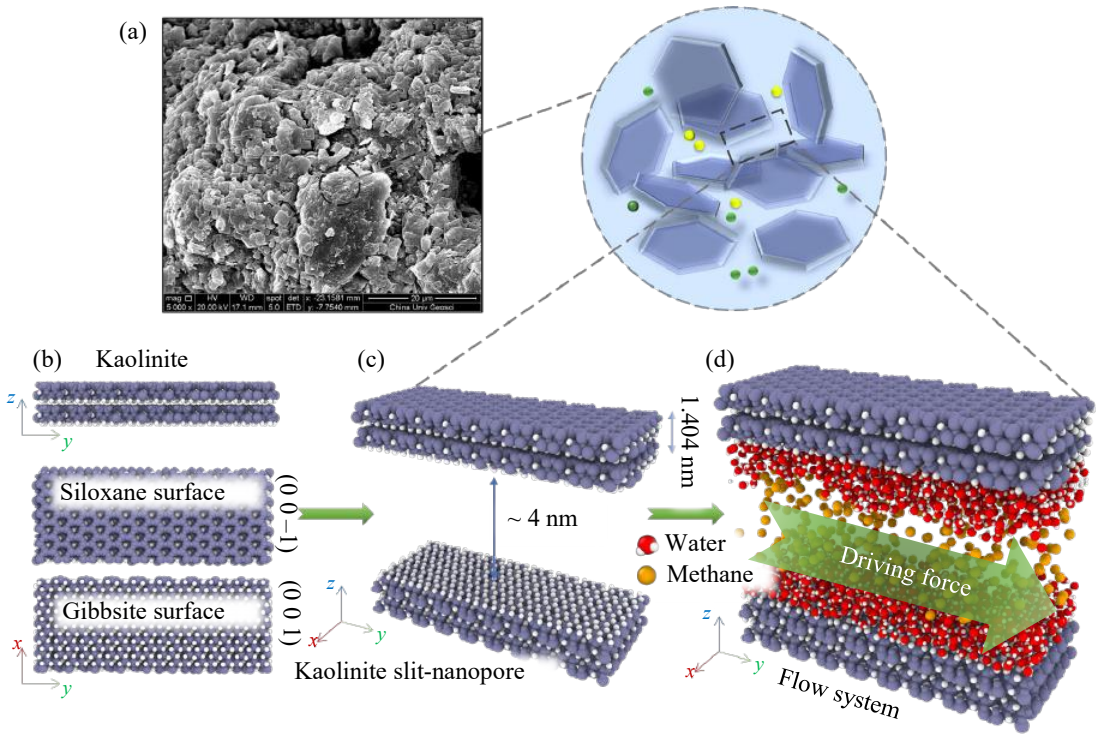

Fig. 1. (a) High-resolution SEM image of clay mineral; (b) two types of kaolinite surface (siloxane and gibbsite surface); (c) nanopore built by two kaolinite sheets and (d) initial MD simulation configuration.

gas excludes the velocity component in this direction; ∇p_y represents the pressure difference along the y-axis, MPa; 3, 6, 9 MPa are selected in our simulations. In the MD simulations, it is common practice and a necessary choice to impose a substantial pressure differential, primarily to achieve an observable nanoflow within the nanosecond-scale simulation timeframe, even if the pressure difference across the ends of the pore deviates from actual conditions (Zhan et al., 2020; Xu et al., 2022; Fang et al., 2024).

2.3 Force fields and simulation details

In this study, the CLAYFF (Cygan et al., 2004) force field and flexible SPC water model (Amira et al., 2004) were used to model kaolinite substrates and water molecules, respectively. This combination of force fields enables us to accurately capture the fluid–solid interactions that are critical for investigating water/gas flow in nanoporous media. The OPLS-UA (Martin and Siepmann, 1998) force field was used to descript methane molecules. The specific parameters used in these force fields can be found in Table S2 of the Supplementary file.

Simulation tasks were executed using the LAMMPS package (Plimpton, 1995). The atoms in kaolinite mineral sheets are kept rigid with the exception of H atoms in hydroxyl groups in all MD simulations. The van der Waals forces were represented by the Lennard-Jones potential, while the Lorentz–Berthelot combining rules were applied to determine cross-interactions between unlike atoms (Allen and Tildesley, 1987). A cutoff distance of 1.0 nm was employed to evaluate short-range nonbonded effects, encompassing both van der Waals and Coulombic components. For long-range electrostatic calculations, the particle–particle/particle–mesh (PPPM) algorithm was adopted, ensuring a precision of 10^{-4} (Eastwood et al., 1984). A canonical NVT ensemble was used in simulations where the temperature is controlled by the Nosé-Hoover thermostat (in EMD simulations, temperature coupling occurs in all three xyz directions; in the EF-NEMD simulations, temperature coupling was applied only in the xz directions) (Nose, 1984). Periodic boundary conditions were used in all directions.

3. Results and discussion

3.1 Single-phase water distribution

The differential affinity of water for the two surfaces of kaolinite has been widely acknowledged; the hydroxylated gibbsite surface displays a strong affinity for water, demonstrating hydrophilic properties, whereas the interaction between the siloxane surface and water is weak and characterized as relatively hydrophobic (Zhang et al., 2016; Shi et al., 2023). Fig. 2(a) illustrates the mass density of water in nanopores along the z-axis in the NPss, NPgg and NPsg simulation systems, with water molecules fully occupying the pore space in the absence of methane molecules ($S_w = 1.0$). In the NPss and NPgg systems, water molecules form centrally symmetric distributions due to interactions with the solid surfaces, with two layers of water molecules near the surfaces. The first water layer has a high density of 2-3 g/cm^3, much higher than the liquid-phase water density of 1 g/cm^3, with a single hydrogen bond length ($\sim$ 3.2 Å) between the first and second layers.

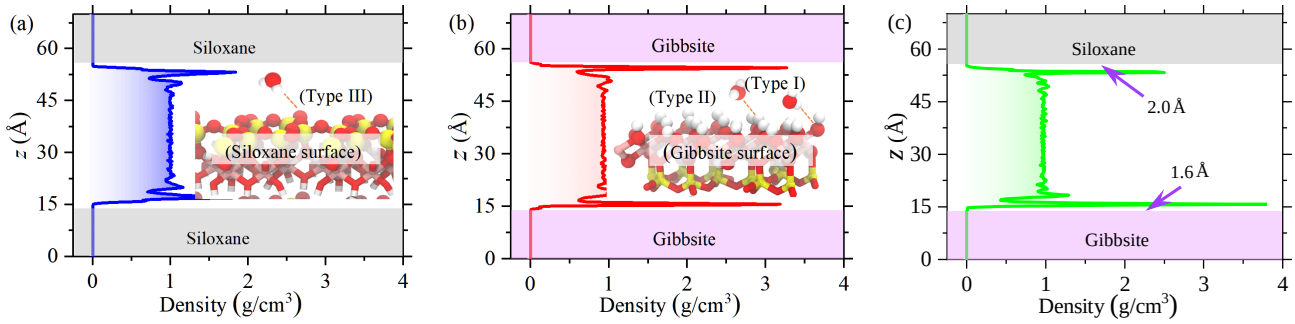

Fig. 2. Mass density of water in nanopores along z-axis in the three simulation systems of (a) NPss, (b) NPgg and (c) NPsg.

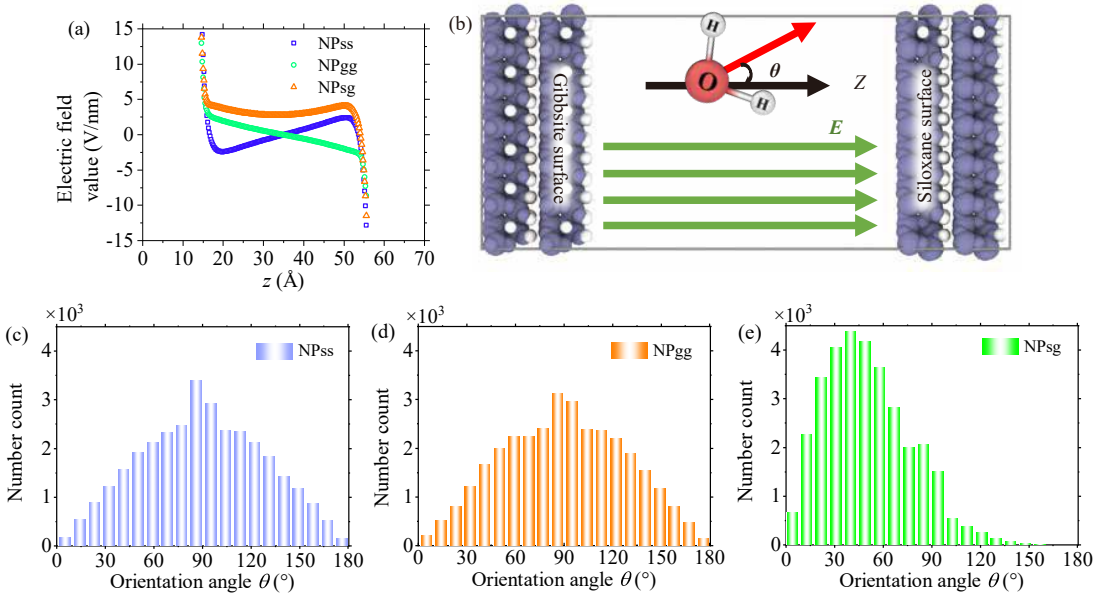

Fig. 3. (a) Electric field distribution in the center of the surface in the *xy* plane along the *z* direction in the three models with empty pore space. (b) Schematic diagram of electric field in NPsg system. Histogram of water molecular orientation angle distribution in the (c) NPss, (d) NPgg and (e) NPsg simulation systems at equilibrium state.

Compared to the siloxane surface (Fig. 2(a)), the hydroxylated gibbsite surface (Fig. 2(b)) displays a more pronounced affinity for hydrogen bonding with water molecules, leading to a higher density of the water layer. In the NPss system, the first hydration layer peak is located 2.0 Å from the siloxane surface, whereas in the NPgg system, the peak is closer at 1.6 Å from the gibbsite surface. These results are attributed to the presence of hydroxyl groups on the gibbsite surface, which form hydrogen bonds with water molecules (types I and II in Fig. 2(b)), in contrast to the siloxane surface, where only some oxygen atoms form hydrogen bonds with water (type III in Fig. 2(a)).

In the NPsg simulation system where the pore substrates consist of both gibbsite and siloxane surfaces, the distribution of water molecules exhibits significant spatial heterogeneity and a non-centrosymmetric pattern (Fig. 2(c)), contrasting with nanopores featuring a single type of basal substrate. The density of water molecules near the gibbsite surface is significantly higher than that near the siloxane surface. This is due to the abundant hydroxyl groups on the gibbsite surface, which form strong hydrogen bonds with water molecules and promote adsorption. The first water layer on both solid surfaces exhibits significantly higher strength, a phenomenon influenced by the electrostatic field within pores. Given the small pore size, the distribution of surface charges is uneven, resulting in disparate distributions of the electrostatic field. In the NPsg system, the electrostatic field points from the positively charged gibbsite surface toward the relatively less charged siloxane surface, with a field strength of approximately 2.5 V/nm at the center of the pore (Figs. 3(a) and 3(b)). This strong, asymmetric field not only enhances water adsorption at the gibbsite surface but also induces a preferred orientation of water dipoles (Xiong et al., 2020b). As shown in Figs. 3(c) and 3(d), in the NPss and NPgg systems where the electrostatic field is symmetrically distributed along the *z*-axis and much weaker in magnitude, the angle between the water dipole moment and the *z*-axis follows a normal distribution with a peak at approximately 90°, indicating that the water dipoles tend to align parallel to the *xy* plane. In contrast, in the NPsg system, the dipole orientation exhibits a peak

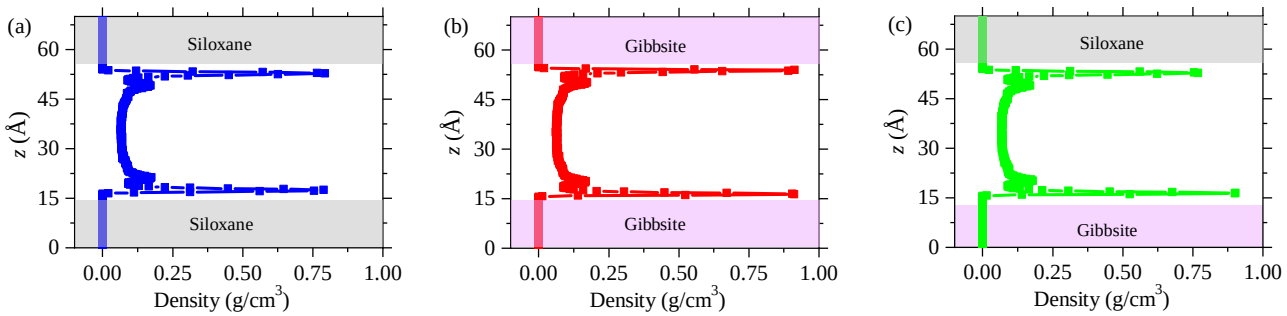

Fig. 4. Mass density of methane in nanopores along the z-axis in the three MD simulation systems of (a) NPss, (b) NPgg and (c) NPsg.

at around 40° (Fig. 3(e)), aligning with the direction of the electrostatic field. This indicates that the electrostatic field plays a dominant role in inducing water dipole orientation to minimize the electrostatic potential energy of the system.

3.2 Single-phase methane distribution

In the case where only gas molecules are present in the pores ($S_w = 0$), the density distribution of methane molecules along the z-axis is mirror-symmetrical in pores composed of a single type of substrate (Figs. 4(a) and 4(b)); meanwhile, in the NPsg system, it is asymmetric (Fig. 4(c)). There are two adsorption layers of methane on both sides of the clay pore wall due to the stronger interaction between CH_4-solid compared to the CH_4-CH_4 intermolecular interaction: a first strong adsorption layer and a second weaker one. The thickness of the methane adsorption layer (3.7 Å) is approximately equal to its molecular length parameter in the Lennard-Jones potential, corroborating the finding of Zhao et al. (2024) and Hao et al. (2018). As the interactions weaken, methane density stabilizes further from the pore wall. In the absence of water, methane adsorption on the gibbsite surface is stronger than that on the siloxane surface. The first adsorption peak also occurs closer to the gibbsite surface due to stronger van der Waals interactions. Overall, methane adsorption on both surfaces of kaolinite is strong, while it varies in intensity and interaction mode depending on the surface characteristics.

3.3 Two-phase water/gas distribution

The distribution of gas/water molecules at different water saturation levels (0.1-0.5) are depicted for the three simulation systems in Fig. 5. The results show that the distribution of water/gas within nanopores is strongly correlated with the surface properties of the pores (wettability) and water saturation. In the NPss system, characterized by the hydrophobic siloxane surface of pore walls, water clusters form and adhere to the solid surface at a water saturation level of 0.1. As the saturation level increases to 0.2, water molecules form a water bridge between the two solid surfaces, with the thickness of the water bridge increasing proportionally. When the water saturation increases to 0.2, the presence of a water bridge can block the connectivity of gases on both sides completely, which can also be referred to as a "water lock" (Zheng et al., 2023). Beyond the water bridge, no water molecules are adsorbed in the remaining surface area. In the NPgg system where the pores are composed of hydrophilic gibbsite surfaces, at low water saturation ($S_w < 0.4$), water molecules are uniformly distributed along the pore walls, consistent with previous findings on the distribution of water molecules on hydrophilic solid surfaces (Xu et al., 2020; Zheng et al., 2025). When the water saturation level reaches 0.4, a "water lock" forms aside from the water bridges and the remaining hydroxylated hydrophilic surfaces are covered by adsorbed water molecules, which contrasts with the behavior observed in the NPss system. In the NPsg simulation system (Janus pores), the different composition of pore base surfaces results in the presence of an electrostatic field along the z-axis-positive direction within the pore (Fig. 3(b)). This phenomenon, coupled with the action of water surface tension, leads to the formation of multiple independent water bridges within the pore, a characteristic also observed in illite pores (Xiong and Devegowda, 2022). As the water saturation level increases, the volume of water bridges rises, gradually merging into a "water lock".

The density distribution of gas and water molecules along the z-axis in the three systems under different saturation conditions is depicted in Fig. 6. In each system, a layer of water molecules on the solid surface persists due to the interaction of solid and water. In the NPss and NPsg systems, the density of the water layer on the solid surface increases with the water saturation level within the pore. In contrast, in the NPgg system, the density of the water layer remains unchanged with varying water saturation levels, consistent with the conditions where water fully occupies the space (as shown in Fig. 2(b)). In these hydrophilic pores, water molecules preferentially adsorb onto the pore walls, as shown in Fig. 5(b). Even under conditions of high water saturation where water bridges form, surface adsorption remains unaffected, which results in a consistently high density of the adsorbed water layer across all levels of water saturation. These simulation results reflect the strong interaction between the hydrophilic surface and water molecules. In the NPss and NPgg systems, the water density distribution along the z-axis is symmetrical, while in the NPsg system, the adsorption density of water on the solid surface correlates with the surface properties. It should be noted that at low water saturation ($S_w = 0.1$) in the NPgg system, due to the limited number of water molecules (Fig. 5(b)), an asymmetric

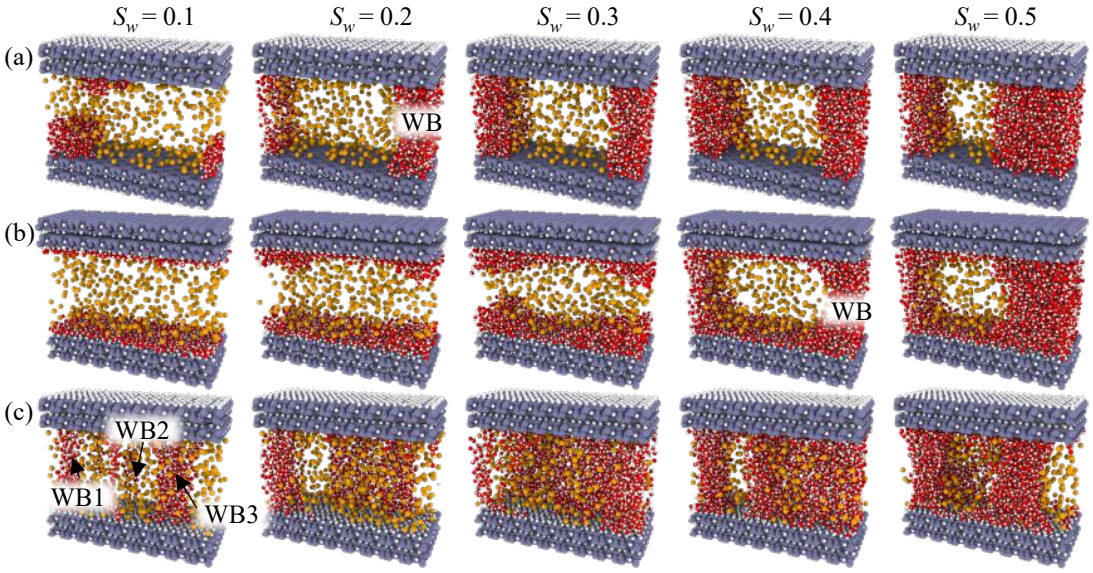

Fig. 5. Gas/water two-phase equilibrium configurations in slit nanopores in the three different systems at different water saturations based on MD simulations: (a) NPss, (b) NPgg and (c) NPsg (WB stands for water bridge).

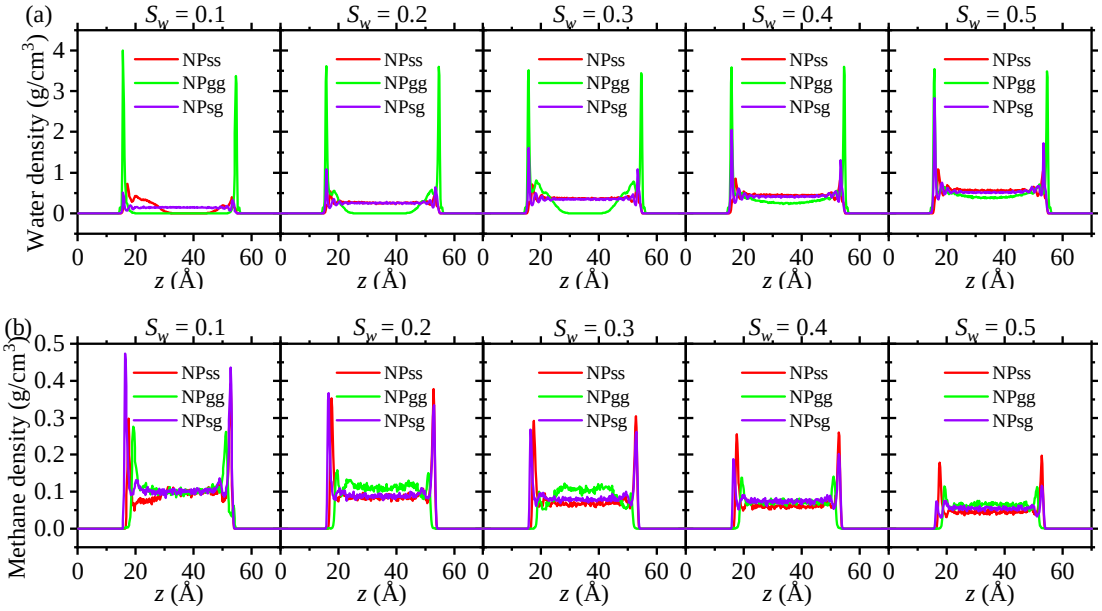

Fig. 6. (a) Water and (b) methane density distribution along the z direction in the three MD simulation systems at different water saturations.

density distribution across the pore is likely to occur.

As shown in Fig. 6(b), the distribution of methane molecules is strongly correlated with that of water molecules within the pores. In the NPss and NPsg systems, under the simulated water saturation conditions in pores ($S_w \leq 0.5$), the pore walls are not fully occupied by water molecules, leaving space for the adsorption of a certain amount of methane. As water saturation increases, the methane adsorption density on the pore walls decreases. In the hydrophilic NPgg system, before water bridges form, methane is primarily concentrated in the central region of the pores. After the formation of water bridges, methane molecules accumulate on both sides of the pore walls. In contrast, under the same water saturation conditions, the methane density on hydrophobic surfaces is higher than that on hydrophilic surfaces. Additionally, compared to hydrophobic surfaces, the water layer on hydrophilic surfaces is closer to the pore wall, while the methane adsorption layer is relatively farther away.

3.4 Single-phase flow

Firstly, the fluid characteristics of a single phase (water or gas) within the nanopores are discussed. When the water saturation S_w reaches 1.0, meaning that water molecules fully occupy the pore space, by employing nonequilibrium MD si-

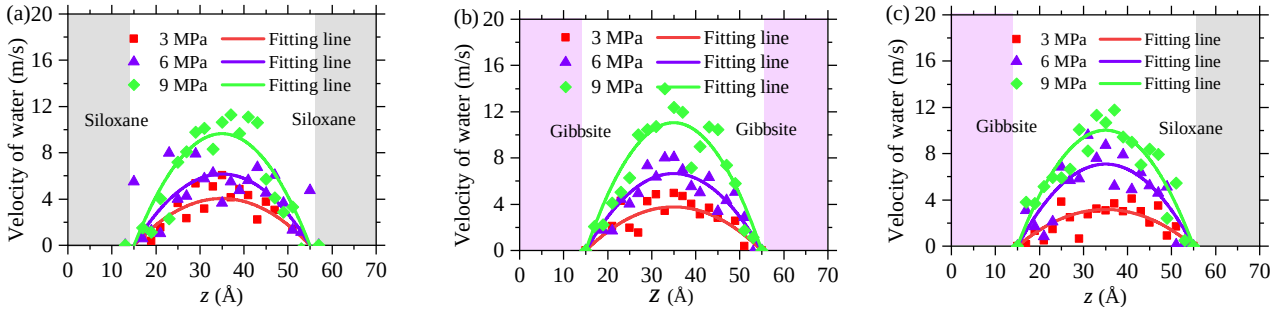

Fig. 7. Velocity distribution of water molecules along the z direction in the three simulation systems at different pressure differences, where the velocity is the average of all MD systems: (a) NPss, (b) NPgg and (c) NPsg.

Table 1. Calculation results for H_2O and CH_4 effective mean viscosity and slip length in the three simulation.

Molecules	Systems	η (Pa·S)	L_s (Å)
H_2O	NPss	0.087 ± 0.01	/
	NPgg	0.083 ± 0.004	/
	NPsg	0.089 ± 0.004	/
CH_4	NPss	0.00586 ± 0.0004	21.48 ± 0.8
	NPgg	0.00648 ± 0.001	27.34 ± 2.25
	NPsg	/	/

mulations with an external field, the water molecules undergo directional movement along the y-axis under the influence of external driving forces. The steady-state velocity distribution of water molecules along the z-axis within the pore space under different pressure differentials can be obtained, as shown in Fig. 7. Due to the thermal motion of water molecules, there are significant velocity fluctuations, but the overall movement of the water molecules is aligned with the direction of the external field (y-direction). The interaction between the solid interface and the water molecules results in lower velocities for water molecules near the solid interface. In contrast, water molecules at the pore center exhibit higher velocities. Thus, the velocity distribution of a pressure-driven water flow in a pore can be described by Poiseuille-like flow. The greater the pressure difference across the sides of the pore is, the more pronounced the directional movement trend of the water molecules.

The velocity profile in the bulk region follows a parabolic curve. For water, the no-slip boundary condition applies due to strong water–solid interactions and weak driving force (Wu et al., 2017), The effective slit widths of nanopores with different mineral compositions fit well to a quadratic function of z (Zhang et al., 2021b):

$$v(z) = a\left(z - \frac{L_z}{2}\right)^2 + b \tag{3}$$

where a and b represent fitting parameters; $v(z)$ denotes the velocity along the z-direction, m/s; L_z represents the length of the pore along the z-axis, Å, and z is the coordinate along the z-direction, Å. Apparent viscosity (η) can be obtained by Eq. (4) and is shown in Table 1:

$$\eta = \frac{-\nabla p}{2a} \tag{4}$$

Using the same method, the velocity distribution of methane molecules along the z-axis was obtained under different pressure differences within the three pore types fully occupied by methane molecules ($S_w = 0$), as shown in Fig. 8. Compared to liquid water molecules, gaseous methane molecules are more easily driven and their velocities are over an order of magnitude higher. The velocity distribution trend along the z-axis is similar to that of water molecules, with lower velocities near the solid surface and higher velocities at the center of the pore. However, a notable difference is the presence of slip for gas molecules at the solid surface. The interaction between methane molecules and the solid surface is limited to van der Waals forces, which are weaker compared to the hydrogen bonding between water molecules and the solid surface.

Notably, under the same pressure difference, the velocity of methane molecules varies across different pore types. Methane molecules in the NPgg system exhibit the highest velocities, followed by the NPsg system, with the NPss system showing the lowest directional movement. This is primarily because the gibbsite surface has a more uniform atomic distribution than siloxane, which likely leads to a more uniform distribution of potential barriers or energy wells, as illustrated in the 2D contour maps of surface-methane interaction energy in Fig. 8(d) (siloxane surface) and Fig. 8(e) (gibbsite surface). Such uniformity facilitates the directional movement of methane molecules and results in a weaker directional confinement effect on them. In the NPsg simulation system, methane molecules near the hydrophilic gibbsite surface exhibit higher velocities than those near the siloxane surface, and this trend is also evident when comparing the other two systems.

In pores with a single wettability surface (NPss and NPgg systems), the velocity distribution of methane molecules along the z-axis shows good axial symmetry. Viscosity is influenced by the friction between methane molecules and the nanopore walls, causing significant velocity differences between the pore center and the wall region. In NPsg Janus pores, the difference in hydrophilic and hydrophobic surface properties

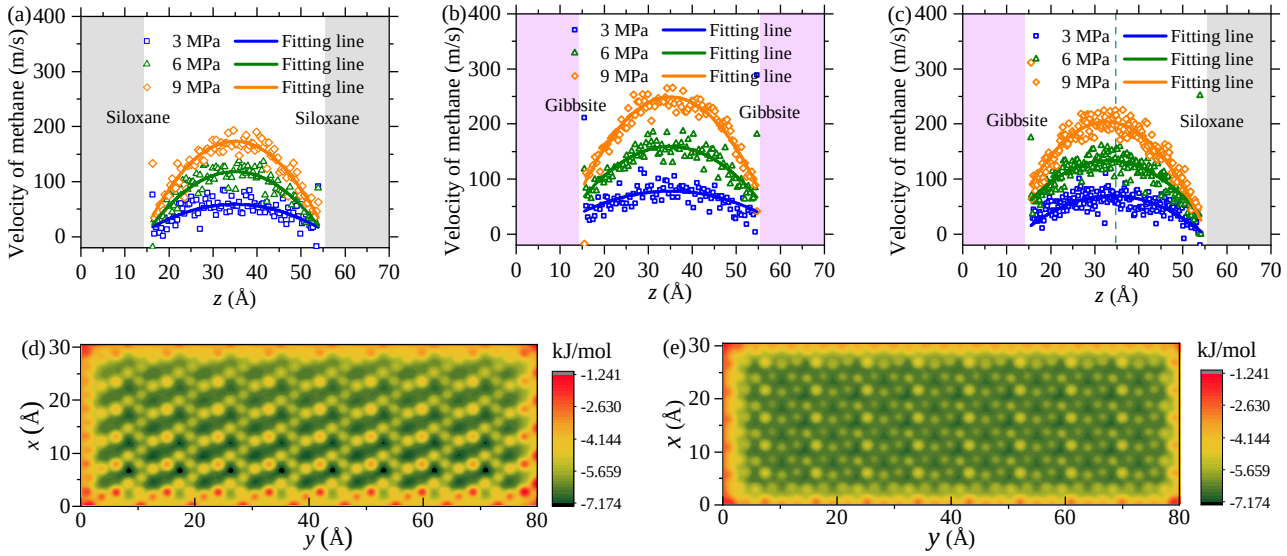

Fig. 8. Velocity distribution of methane along the z direction in the three simulation systems under different pressure differences: (a) NPss, (b) NPgg, (c) NPsg, (d) total siloxane-CH_4 and (e) gibbsite-CH_4 interaction energy contour maps, with CH_4 molecules located at the peak of the first methane shell layer on the surface.

leads to a variation in frictional interactions with methane molecules, creating an asymmetric velocity distribution along the z-axis (Fig. 8(c)). As shown in Figs. 8(a) and 8(b), the no-slip boundary condition is evidently inapplicable to methane flow (Squires and Quake, 2005). To determine the appropriate boundary conditions for the system and reveal the intrinsic relationship between solid surface properties and slip behavior, the slip length of methane molecules at different interfaces was calculated. To this end, slip length is defined as the distance over which the fluid velocity remains stable within the surface/wall region, expressed as follows (Owusu et al., 2023):

$$L_s = \pm \frac{v_y z_s}{\left(\frac{\mathrm{d}v_y}{\mathrm{d}z}\right)_{z_s}} \tag{5}$$

where v_y represents the slip velocity at the solid-gas boundary, m/s; $(\mathrm{d}v_y/\mathrm{d}z)_{z_s}$ represents the location of the slip surface, Å, and is the derivative of the slip velocity at the slip surface, s^{-1}; L_s stands for the slip length, Å, and the calculated values are shown in Table 1.

As shown in Table 1, within the same pore, the viscosity of methane gas is significantly lower than that of water molecules. For water molecules, due to the application of the no-slip boundary condition, the viscosity coefficient in pores with different surface properties shows slight variations, which can be attributed to the strong solid-liquid interactions. However, for methane gas, the viscosity differs for pore walls of varying surface properties, directly affecting the slip length of methane molecules along the pore walls. In single-phase gas flow, the slip length of methane molecules on hydrophilic surfaces is significantly greater than that on relatively hydrophobic pores. This suggests that the potential or energy barrier distribution on hydrophilic surfaces is likely more uniform, facilitating the formation of a larger slip length. In contrast, relatively hydrophobic surfaces may exhibit stronger local variations in potential fields or energy wells that hinder the slippage of gas molecules.

3.5 Two-phase flow

To quantitatively examine gas flow driven by pressure differences through pores with varying hydrophobicity and hydrophilicity under different water saturation conditions, the average velocity of water and gas molecules along the pore direction (y-axis) in the three simulated systems was calculated, as shown in Fig. 9. The results show that the movement velocity of gas molecules is closely related to the formation of water bridges, while water molecules, due to their strong interactions with the pore walls, exhibit almost no directional movement under the simulated conditions. For the NPss and NPgg systems, at low saturation levels (before the formation of water bridges, NPss: $S_w \leq 0.1$; NPgg: $S_w \leq 0.3$), the average velocity of methane molecules increases linearly with the pressure difference across the pores. As water saturation (S_w) increases, the frictional effects on gas molecules become more pronounced, resulting in a decrease in their directional movement velocity. Once water bridges form due to a higher water saturation, gas movement becomes hindered, and under the pressure differentials used in the simulations, directional movement is essentially prevented. When $S_w = 0.1$, in the NPss system, water molecules aggregate on the solid surface to form water clusters (Fig. 5(a)), obstructing part of the gas movement. In contrast, in the NPgg system, water molecules are uniformly distributed on the solid surface (Fig. 5(b)), causing less interference with the gas molecules. Consequently, under the same water saturation and pressure differential, gas molecules exhibit a higher velocity in the NPgg system. In the NPsg system, multiple water bridges form in the pores even at low saturation, impeding gas movement but

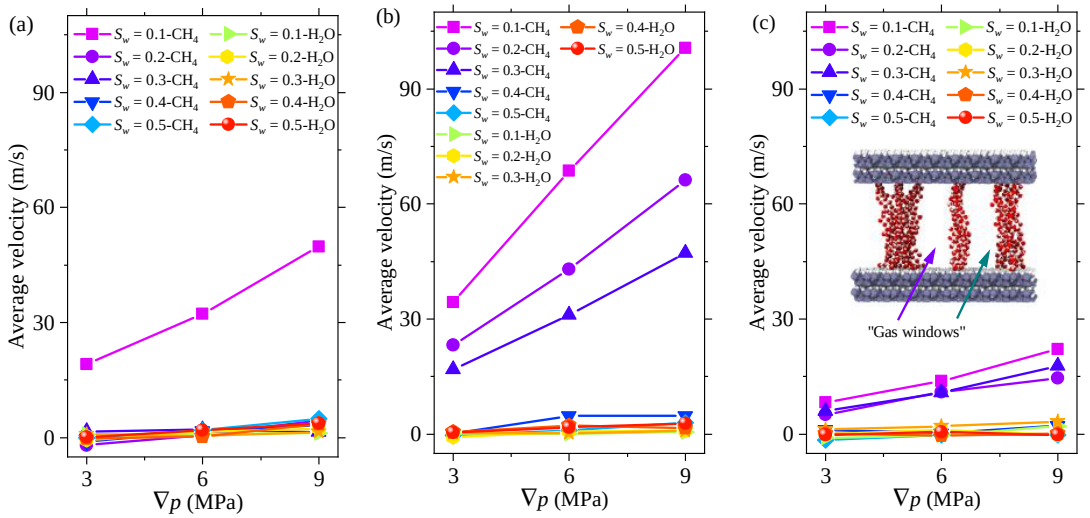

Fig. 9. Average velocity of water and gas molecules within nanopores under varying pressure differences and water saturation conditions in the three simulation systems: (a) NPss, (b) NPgg and (c) NPsg.

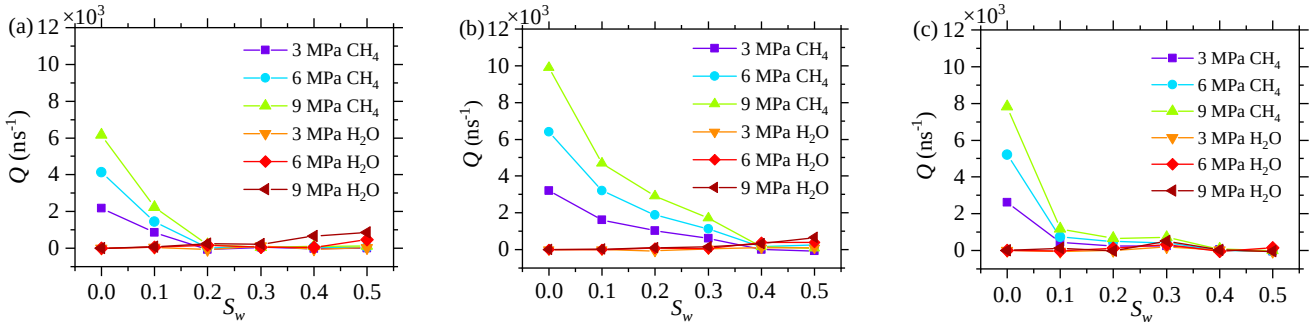

Fig. 10. Flux of water and methane at different pressure differential under different water saturation conditions in the three simulation systems: (a) NPss, (b) NPgg and (c) NPsg.

leaving "gas windows" through which some gas can still flow. As water saturation increases, the size of the water bridges also increases, eventually blocking the pores completely and preventing the directional movement of gas molecules.

Furthermore, the gas/water flux is defined as the average number of molecules passing through a cross-sectional area of a pore per unit time. Once the gas flow stabilizes, the flux Q is related to the density and velocity distribution along the z-axis:

$$Q_i = \frac{1}{L_y}\int \rho_{n,i}(z)v_{y,i}(z)\mathrm{d}z, i = w, m \tag{6}$$

where $\rho_{n,w}(z)$, $\rho_{n,m}(z)$ represent water and methane number 1D density along the z-axis, respectively, m^{-1}; $v_{y,w}(z)$, $v_{y,m}(z)$ represent the y direction water and methane velocity distribution in the z direction, m/s (Zhang et al., 2021b). By employing statistical averaging methods to calculate the flow rate of water and gas molecules within the pores, computational errors can be effectively reduced. The simulation results for the flow rates of water and methane under different pressure differences in the three simulation systems are shown in Fig. 10.

Under the same pore and water saturation conditions, the flux of water molecules remains nearly zero and the molecules stay almost stationary under the same pressure difference, in contrast to gas molecules, as illustrated in Fig. 10. The viscosity of water molecules is much higher than that of gas molecules, resulting in nearly zero water flux. In contrast, gas flux increases with the pressure difference and is influenced by surface properties and water saturation. As saturation increases, gas flux decreases due to reduced pore space and water bridge formation. In the NPss system, gas flow nearly halts when $S_w = 0.2$ due to water lock formation (Fig. 5(a)). In the NPgg system, flow only stops at $S_w = 0.4$, as water molecules occupy the solid surface, leaving more space for gas transport until water lock forms (Fig. 5(b)). In the NPsg system, gas flow decreases rapidly at low saturation ($S_w < 0.1$), then more slowly until $S_w = 0.4$, when the pore is blocked. Multiple water bridges in Janus pores hinder gas flow but allow partial transport until full blockage (Fig. 5(c)). Overall, pore surface properties control water bridge formation and gas flow rates.

The permeability K of a single-phase system p with viscosity η_p is given by the following expression, as described by Darcy's law:

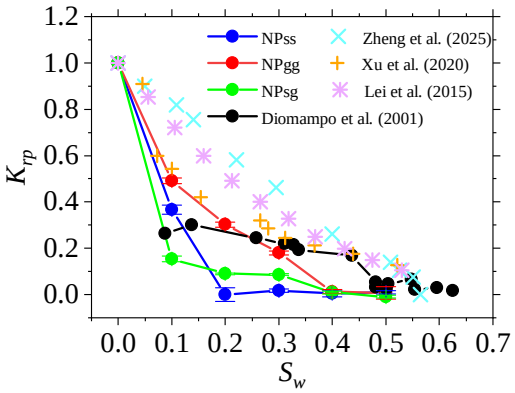

Fig. 11. Relative permeability of three types of nanopores for methane gas at under different water saturations, along with relevant experimental and simulation results from previous studies for comparison.

$$K = \frac{\eta_p Q_{sp} L_y}{A_{xz} \nabla P} \tag{7}$$

where Q_{sp} represents the flux of single-phase p, ns^{-1}; L_y represents the length of the pore in the y direction, Å; A_{xz} represents the cross-section of the nanopore, $Å^2$; ∇P is the pressure differential, MPa; In a multiphase system, the relative permeability K_{rp} of a single phase is expressed as:

$$K_{rp} = \frac{Q_{mp}}{Q_{sp}} \tag{8}$$

where Q_{mp} denotes the flux of phase p in the multiphase system.

Taking the above formula as a basis, the relative permeability of gas molecules transported in different types of nanopores under various water saturation conditions was calculated, as shown in Fig. 11. It can be observed that the overall trend of gas relative permeability decreasing with rising water saturation in this study is generally consistent with previous results, including Diomampo's experimental data (Diomampo, 2002) and the simulation results reported by Lei et al. (2015), Xu et al. (2020) and Zheng et al. (2025). The relative permeability of gas decreases with increasing water saturation within the pores. In real sedimentary environments, the gas relative permeability is the combined result of multiple surface wettability interactions in the pore structure. In hydrophilic systems, the relative permeability decreases slowly with increasing water saturation. In the relatively hydrophobic NPss system, the relative permeability decreases rapidly, while in the NPsg system, it first decreases rapidly and then slowly drops to zero. Under low water saturation conditions ($S_w < 0.2$), the order of relative permeability is NPgg > NPss > NPsg. When water saturation increases ($0.2 < S_w < 0.4$), the order of relative permeability is NPgg > NPsg > NPss. This trend is consistent with the changes in gas flow rates described above. Overall, the gas transport efficiency is higher in hydrophilic pores because water preferentially wets the pore walls, leaving larger and more continuous gas pathways through the pore centers, reducing capillary resistance and facilitating gas flow. In contrast, in hydrophobic pores, water tends to accumulate in the pore centers, which blocks gas channels and significantly reduces gas permeability. In Janus pores, the formation of multiple water bridges partially hinders gas transport. In the experimental measurements, which are based on macropores ranging from micrometers to millimeters in size, the capillary forces within the macropores are relatively small, allowing water molecules to move more easily without forming water locks. Therefore, under the same water saturation conditions, the experimentally measured relative permeability of natural gas is relatively higher compared to the simulation results.

4. Conclusions

This study systematically investigated the two-phase transport behavior of gas and water in hydrophilic, relatively hydrophobic, and Janus nanopores during gas extraction from hydrate-bearing sediments. Multiphase molecular models considering different water saturations were constructed using GCMC + MD, and EMD and EF-NEMD simulations were performed to explore phase distributions and flow characteristics. The main findings can be summarized as follows:

1) In pure gas or water systems, adsorption layers form on the pore walls. In Janus pores, the internal electric field modifies the arrangement of water molecules, producing distinct gas-water distributions under two-phase conditions.
2) Water lock formation pathways vary with wettability. Hydrophilic pores favor surface adsorption at low saturations ($S_w < 0.4$), with bridges evolving from films to water locks as saturation increases. In relatively hydrophobic pores, water clusters form at low saturations before transitioning to water locks. In Janus pores, the electric field promotes multiple independent water bridges at low saturations, and these merge into water locks at higher saturations.
3) Water bridges significantly impede gas transport, while water locks block it entirely. At the same S_w and pore size, hydrophilic pores support more efficient gas flow. In relatively hydrophobic and Janus pores, bridges form at lower S_w, reducing gas permeability; however, some transport is maintained in Janus pores via gaps between unconnected bridges.

Overall, this study reveals how water saturation, pore wall properties, pressure gradient, and water bridge formation collectively control water/gas permeability at the nanoscale, providing valuable molecular-scale insights into gas and water flow behaviors within nanopores. These findings are directly relevant to hydrate-bearing reservoir engineering, as they demonstrate how pore surface wettability influences gas production efficiency. Such insights can guide strategies for reservoir modification or wettability alteration to enhance gas recovery.

Acknowledgements

This work was supported by the National Natural Science Foundation of China (Nos. 42206235, 42466009 and 42306240), the Engineering Research Center of Rock-Soil Drilling & Excavation and Protection Open Fund (No.

202403), and the High-level Talent Research Start-up Fund Project of Hainan University (No. XJ2400009212).

Supplementary file

https://doi.org/10.46690/ager.2025.07.02

Conflict of interest

The authors declare no competing interest.

References

Allen, M. P., Tildesley, D. J. Computer Simulation of Liquids. New York, USA, Oxford University Press, 1987.

Amira, S., Spångberg, D., Hermansson, K. Derivation and evaluation of a flexible SPC model for liquid water. Chemical Physics, 2004, 303(3): 327-334.

Boswell, R. Is gas hydrate energy within reach? Science, 2009, 325(5943): 957-958.

Cai, J., Xia, Y., Lu, C., et al. Creeping microstructure and fractal permeability model of natural gas hydrate reservoir. Marine and Petroleum Geology, 2020, 115: 104282.

Collett, T., Bahk, J. J., Baker, R., et al. Methane hydrates in nature-current knowledge and challenges. Journal of Chemical Engineering Data, 2015, 60(2): 319-329.

Cygan, R. T., Liang, J. J., Kalinichev, A. G. Molecular models of hydroxide, oxyhydroxide, and clay phases and the development of a general force field. Journal of Physical Chemistry B, 2004, 108(4): 1255-1266.

Daigle, H., Cook, A., Malinverno, A. Permeability and porosity of hydrate-bearing sediments in the northern Gulf of Mexico. Marine and Petroleum Geology, 2015, 68: 551-564.

Dendy, S. E., Koh, C. A. Clathrate Hydrates of Natural Gases. Boca Raton, USA, CRC Press, 2007.

Diomampo, G. P. Relative permeability through fractures. Stanford, Stanford Geothermal Workshop, 2002.

Downs, R. T., Hall-Wallace, M. The American Mineralogist crystal structure database. American Mineralogist, 2003, 88(1): 247-250.

Eastwood, J. W., Hockney, R. W., Lawrence, D. N. P3M3DP-the three-dimensional periodic particle-particle/particle-mesh program. Computer Physics Communications, 1984, 35: 618-619.

Eric, L., Marcia, H., Mark, M. NIST Standard Reference Database 23: Reference Fluid Thermodynamic and Transport Properties-REFPROP, Version 9.1. Gaithersburg, USA, National Institute of Standards and Technology, 2013.

Fang, B., Lü, T., Li, W., et al., Microscopic insights into poly- and mono-crystalline methane hydrate dissociation in Na-montmorillonite pores at static and dynamic fluid conditions. Energy, 2024, 288: 129755.

Fang, X., Yang, D., Ning, F., et al. Experimental study on sand production and coupling response of silty hydrate reservoir with different contents of fine clay during depressurization. Petroleum, 2023, 9(1): 72-82.

Falk, K., Sedlmeier, F., Joly, L., et al. Molecular origin of fast water transport in carbon nanotube membranes: Superlubricity versus curvature dependent friction. Nano Letters, 2010, 10(10): 4067-4073.

Hao, Y., Jia, X., Lu, Z., et al. Water film or water bridge? Influence of self-generated electric field on coexisting patterns of water and methane in clay nanopores. Journal of Physical Chemistry C, 2019, 123(36): 22656-22664.

Hao, Y., Yuan, L., Li, P., et al. Molecular simulations of methane adsorption behavior in illite nanopores considering basal and edge surfaces. Energy & Fuels, 2018, 32(4): 4783-4796.

Ho, T. A., Striolo, A. Water and methane in shale rocks: Flow pattern effects on fluid transport and pore structure. AIChE Journal, 2015, 61(9): 2993-2999.

Holditch, S. A. Factors affecting water blocking and gas flow from hydraulically fractured gas wells. Journal of Petroleum Technology, 1979, 31(12): 1515-1524.

Huang, M., Su, D., Zhao, Z., et al. Numerical study of response behaviors of natural gas hydrate reservoir around wellbore induced by water jet slotting. Advances in Geo-Energy Research, 2023, 7(2): 75-89.

Hyodo, M., Li, Y., Yoneda, J., et al. Effects of dissociation on the shear strength and deformation behavior of methane hydrate-bearing sediments. Marine and Petroleum Geology, 2014, 51: 52-62.

Hyodo, M., Yoneda, J., Yoshimoto, N., et al. Mechanical and dissociation properties of methane hydrate-bearing sand in deep seabed. Soils and Foundations, 2013, 53(2): 299-314.

Karniadakis, G., Beşkök, A., Aluru, N. R. Microflows and Nanoflows: Fundamentals and Simulation. New York, USA, Springer, 2005.

Kleinberg, R. L., Griffin, D. D. NMR measurements of permafrost: Unfrozen water assay, pore-scale distribution of ice, and hydraulic permeability of sediments. Cold Regions Science & Technology, 2005, 42(1): 63-77.

Lei, G., Dong, P., Mo, S., et al. A novel fractal model for two-phase relative permeability in porous media. Fractals, 2015, 23(2): 1550017.

Li, X., Wan, Y., Lei, G., et al. Numerical investigation of gas and sand production from hydrate-bearing sediments by incorporating sand migration based on IMPES method. Energy, 2024a, 288: 129556.

Li, X., Xu, C., Zhang, Y., et al. Investigation into gas production from natural gas hydrate: A review. Applied Energy, 2016, 172: 286-322.

Li, X., Xu, S., Hao, Y., et al. Gas transport in shale nanopores with miscible zone. Geofluids, 2020, 2020: 6410614.

Li, Y., Liu, L., Jin, Y., et al. Characterization and development of natural gas hydrate in marine clayey-silt reservoirs: A review and discussion. Advances in Geo-Energy Research, 2021, 5(1): 75-86.

Li, Y., Xu, T., Xin, X., et al. Multi-scale comprehensive study of the dynamic evolution of permeability during hydrate dissociation in clayey silt hydrate-bearing sediments.

Advances in Geo-Energy Research, 2024b, 12(2): 127-140.

Liu, B., Qi, C., Zhao, X., et al. Nanoscale two-phase flow of methane and water in shale inorganic matrix. Journal of Physical Chemistry C, 2018, 122(46): 26671-26679.

Liu, H., Xiong, H., Yu, H., et al. Effect of water behaviour on the oil transport in illite nanopores: Insights from a molecular dynamics study. Journal of Molecular Liquids, 2022, 354: 118854.

Low, P. F. The swelling of clay: II. Montmorillonites. Soil Science Society of America Journal, 1980, 44(4): 667-676.

Lyu, F., Ning, Z., Jia, Z., et al. Investigation on gas/water two-phase flow in quartz nanopores from molecular perspectives. Journal of Molecular Liquids, 2023, 371: 121145.

Madsen, F. T., Müller-Vonmoos, M. The swelling behaviour of clays. Applied Clay Science, 1989, 4(2): 143-156.

Martin, M. G., Siepmann, J. I. Transferable potentials for phase equilibria. 1. United-atom description of *n*-alkanes. Journal of Physical Chemistry B, 1998, 102(14): 2569-2577.

Nosé, S. A unified formulation of the constant temperature molecular dynamics methods. Journal of Chemical Physics, 1984, 81(1): 511-519.

Owusu, J. P., Karalis, K., Prasianakis, N. I., et al. Diffusion and gas flow dynamics in partially saturated smectites. Journal of Physical Chemistry C, 2023, 127(29): 14425-14438.

Plimpton, S. Fast parallel algorithms for short-range molecular dynamics. Journal of Computational Physics, 1995, 117(1): 1-19.

Qin, X., Liang, Q., Ye, J., et al. The response of temperature and pressure of hydrate reservoirs in the first gas hydrate production test in South China Sea. Applied Energy, 2020, 278: 115649.

Shi, K., Chen, J., Pang, X., et al. Wettability of different clay mineral surfaces in shale: Implications from molecular dynamics simulations. Petroleum Science, 2023, 20(2): 689-704.

Squires, T. M., Quake, S. R. Microfluidics: Fluid physics at the nanoliter scale. Reviews of Modern Physics, 2005, 77(3): 977-1026.

Uchida, S., Klar, A., Yamamoto, K. Sand production model in gas hydrate-bearing sediments. International Journal of Rock Mechanics and Mining Sciences, 2016, 86: 303-316.

Wu, K., Chen, Z., Li, J., et al. Wettability effect on nanoconfined water flow. Proceedings of the National Academy of Sciences of the United States of America, 2017, 114(13): 3358-3363.

Xiong, H., Devegowda, D. Fluid behavior in clay-hosted nanopores with varying salinity: Insights into molecular dynamics. SPE Journal, 2022, 27(3): 1396-1410.

Xiong, H., Devegowda, D., Huang, L. Oil-water transport in clay-hosted nanopores: Effects of long-range electrostatic forces. AIChE Journal, 2020a, 66(8): e16276.

Xiong, H., Devegowda, D., Huang, L. Water bridges in clay nanopores: mechanisms of formation and impact on hydrocarbon transport. Langmuir, 2020b, 36(3): 723-733.

Xu, H., Yu, H., Fan, J., et al. Two-phase transport characteristic of shale gas and water through hydrophilic and hydrophobic nanopores. Energy & Fuels, 2020, 34(4): 4407-4420.

Xu, J., Zhan, S., Wang, W., et al. Molecular dynamics simulations of two-phase flow of n-alkanes with water in quartz nanopores. Chemical Engineering Journal, 2022, 430: 132800.

Yang, M., Zhao, J., Zheng, J., et al. Hydrate reformation characteristics in natural gas hydrate dissociation process: A review. Applied Energy, 2019, 256: 113878.

Ye, J., Qin, X., Xie, W., et al., The second natural gas hydrate production test in the South China Sea. China Geology, 2020, 3(2): 197-209.

Zhan, S., Su, Y., Jin, Z., et al. Effect of water film on oil flow in quartz nanopores from molecular perspectives. Fuel, 2020, 262: 116560.

Zhang, L., Li, Q., Liu, C., et al. Molecular insight of flow property for gas-water mixture (CO_2/CH_4-H_2O) in shale organic matrix. Fuel, 2021a, 288: 119720.

Zhang, L., Lu, X., Liu, X., et al. Surface wettability of basal surfaces of clay minerals: insights from molecular dynamics simulation. Energy & Fuels, 2016, 30: 149-160.

Zhang, M., Guo, G., Tian, H., et al. Effects of italicized angle and turning angle on shale gas nanoflows in non-straight nanopores: A nonequilibrium molecular dynamics study. Fuel, 2020, 278: 118275.

Zhang, W., Feng, Q., Jin, Z., et al. Molecular simulation study of oil-water two-phase fluid transport in shale inorganic nanopores. Chemical Engineering Science, 2021b, 245: 116948.

Zhao, Y., Guan, B., Zhang, T., et al. Molecular insights into multiphase transport through realistic kerogen-based nanopores. Energy & Fuels, 2024, 38(7): 5847-5861.

Zheng, C., Guo, G., Lu, C., et al. Water/methane two-phase flow in the SiO_2 nanoslit can be well described via the deformed water layer model: A molecular simulation study. Geophysical Research Letters, 2025, 52(4): 113458.

Zheng, C., Guo, G., Qin, X., et al. Molecular simulation studies on the water/methane two-phase flow in a cylindrical silica nanopore: Formation mechanisms of water lock and implications for gas hydrate exploitation. Fuel, 2023, 333: 126258.